windshield is coming off the plane at the top of the plot. This complex three-dimensional nature of the fluid flow has significant influence on the heat transfer process between the jet and the inclined surface as well as inside the simulation volume. Higher velocity near the wall causes a local cooling effect as a result of higher convective heat transfer. The temperature contours on the inside surface of the windshield under the heated area in Fig. 5 show an overall comparison between the experimental data (Fig. 2) and CFD prediction of thermal patterns.

The predicted temperature distribution on the inside of the heating pad should also be compared with the experimental data on a point-by-point basis. A detail comparison of predicted and experimental temperature distribution done on 17 points at each of the two constant z lines along the inside of the windshield under the heating pad (Fig. 6). The line $z = 0.7233$ m identifies the central location between the issuing jets, while $z = 0.6076$ m passes through the passenger side jet. Documented results validate the numerical prediction within 1–3°C of the measured temperature values. Corresponding heat transfer coefficients h, computed via Eq. (2), are also plotted in the same figure. The average heat transfer coefficient from the predicted numerical results is $\bar{h} = 25.68$ W/m^2 K.

Conclusions

This Note addressed numerical and experimental studies of a pair of rectangular air jets impinging on an inclined surface. Experimental measurements of surface temperatures, using liquid crystals, yielded a map of local heat transfer coefficients between the surface and the incoming jet for an imposed heat flux. Corresponding three-dimensional numerical simulation has been performed using a finite volume algorithm for obtaining detailed temperature and flow distributions. The numerical simulation correlated reasonably well with the experimental results and further explained the flow characteristics and thermal patterns. A detail comparison of 34 locations under the heating pad validated the numerical predictions within 1–3°C of the measured temperature values. Further investigation should aim for the defogging/defrosting analysis in the flow.

References

[1]Polat, S., Huang, B., Mujumdar, A. S., and Douglas, W. J. M., "Numerical Flow and Heat Transfer Under Impinging Jets: A Review," *Annual Review of Numerical Fluid Mechanics and Heat Transfer*, Vol. 2, 1989, pp. 157–197.

[2]Martin, H., "Heat and Mass Transfer Between Impinging Gas Jets and Solid Surfaces," *Advances in Heat Transfer*, Vol. 13, Academic Press, New York, 1977, pp. 1–60.

[3]Downs, S. J., and James, E. H., "Jet Impingement Heat Transfer—A Literature Survey," American Society of Mechanical Engineers, Paper 87-HT-35, Oct. 1987.

[4]Viskanta, R., "Heat Transfer to Impinging Isothermal Gas and Flame Jets," *Experimental Thermal and Fluid Science*, Vol. 6, No. 2, 1993, pp. 111–134.

[5]Carignano, M., and Pippione, E., "Optimization of Wind-Screen Defrosting for Industrial Vehicles via Computer Assisted Thermographic Analysis," FIJITA Paper 905237, 1990.

[6]Andreone, L., Burzio, G., Damiani, S., and Romitelli, G., "Automatic Measurement of Defrosting/Defogging Process," ATA Paper 92A272, 1992.

[7]Willenborg, K., Foss, J. F., AbdulNour, R. S., McGrath, J. J., and AbdulNour, B. S., "A Model Defroster Flow," *Proceedings of the Eleventh Symposium on Turbulent Shear Flows*, Vol. 2, edited by G. Binder, Centre National de la Recherche, Grenoble, France, 1997, pp. 15.25–15.30.

[8]Nasr, K. J., and AbdulNour, B. S., "Defrosting of Automotive Windshields: Progress and Challenges," *International Journal of Vehicle Design,* Vol. 23. Nos. 3–4, 2000, pp. 360–375.

[9]Johari, H., Pacheco-Tougas, M., and Hermanson, J. C., "Penetration and Mixing of Fully Modulated Turbulent Jets in Crossflow," *AIAA Journal*, Vol. 37, No. 7, 1999, pp. 842–850.

[10]Roy, S., Nasr, K., Patel, P., and Abdulnour, B., "An Experimental and Numerical Study of Heat Transfer off an Inclined Surface Subject to an Impinging Airflow," *International Journal of Heat and Mass Transfer* (to be published).

[11]Yakhot, V., and Orszag, S. A., "Renormalization Group Analysis of Turbulence. I. Basic Theory," *Journal of Scientific Computing*, Vol. 1, No. 1, 1986, pp. 3–51.

[12]Brooks, A. N., and Hughes, T. J. R., "Streamline Upwind/Petrov-Galerkin Formulations for Convection Dominated Flows with Particular Emphasis on the Incompressible Navier–Stokes Equations," *Computer Methods in Applied Mechanics and Engineering*, Vol. 32, No. 1–3, 1982, pp. 199–259.

[13]Patankar, S. V., *Numerical Heat Transfer and Fluid Flow*, Hemisphere, Washington, DC, 1980, pp. 123–126.

[14]Moffat, R. J., "Describing the Uncertainties in Experimental Results," *Experimental Thermal and Fluid Science*, Vol. 1, No. 1, 1988, pp. 3–17.

Numerical Model of the Plasma Jet Generated by an Electrothermal-Chemical Igniter

Michael J. Nusca,* Michael J. McQuaid,† and William R. Anderson‡
U.S. Army Research Laboratory, Aberdeen Proving Ground, Maryland 21005-5066

Introduction

THE electrothermal-chemical (ETC) gun propulsion concept is currently being investigated by the military services. In the ETC gun, energy, which is stored either in batteries or a rotating device, is converted on demand into an electrically generated plasma (resulting from the ablation of polyethylene material in a capillary) that is injected into the chamber of a cannon or gun. This plasma energy is used to ignite the chemical propulsion charge (i.e., solid propellant) as well as to enhance gun performance by taking advantage of a number of unique plasma characteristics. For example, a low-density plasma jet can 1) efficiently ignite charges of high loading density; 2) control propellant mass generation rates[1]; 3) reduce propellant charge temperature sensitivity, that is, the variation of gun performance with changing ambient temperature[2]; and 4) shorten ignition delay, that is, the time interval between firing of the igniter and ignition of the propellant.[3] Because a plasma has a much lower density than the gases generated by a chemical igniter, it has been suggested that energy transport by convection might be as important as radiation transport in plasma-propellant interactions.[4] The plasma is at a temperature that is considerably higher than conventional chemical igniters; thus, radiation effects are nearly 100 times greater than that of chemical igniters (i.e., a T^4 effect). All of these effects can lead to useful improvements in gun performance.

A goal of ETC gun research is to elucidate the relevant physical, mechanical, and chemical mechanisms that underlie the observed ballistic effects. The first phase of the modeling effort involves a time-accurate computational fluid dynamics (CFD) code, which includes high-temperature thermodynamics, variable specific heats and transport properties (viscosity and thermal conductivity), and finite rate (nonequilibrium) chemical kinetics (the chemical mechanism is described in Ref. 5). A separate ETC capillary (i.e., igniter) model,[6] which includes a simulation of electrical currents in the ionized plasma, supplies boundary conditions for the CFD code in terms of the physical and chemical properties of the capillary efflux (plasma). Validation of the capillary model has been reported separately.[6] Validation of the CFD code, including coupled chemistry, is conducted by simulating a series of experiments wherein

Presented as Paper 2000-2675 at the AIAA 31st Plasmadynamics and Lasers Conference, Denver, CO, 19–22 June 2000; received 26 February 2001; accepted for publication 20 September 2001.

*Aerospace Engineer, Weapons and Materials Research Directorate. Associate Fellow AIAA.
†Physical Scientist, Weapons and Materials Research Directorate.
‡Research Chemist, Weapons and Materials Research Directorate.

a plasma jet is generated from an ETC capillary; pressures in the resulting unsteady flowfield are measured using probes mounted on a plate held normal to the efflux.

Multispecies Reacting Flow CFD Code

The high-temperature, nonideal, chemically reacting gas flowfield of the capillary efflux jet is numerically simulated using CFD. The CFD code[7] solves the two-dimensional/axisymmetric, unsteady, real-gas Navier–Stokes equations, including submodels that represent finite rate (nonequilibrium) chemical reactions, multispecies diffusion, as well as variable specific heats, viscosity, and thermal conductivity. The Navier–Stokes equations for two-dimensional/axisymmetric (x, y coordinates) reacting (N species) and unsteady (time, t) flow are written in array form:

$$\frac{\partial U}{\partial t} + \frac{\partial F}{\partial x} + \frac{\partial G}{\partial y} + H = 0 \tag{1}$$

The dependent variables are density ρ, velocity V and components u, v, energy e, and species mass fraction c_i; note that α is the flag for two-dimensional, 0, and axisymmetric, 1, flows:

$$U = \left\{\rho y^{\alpha}, \rho u y^{\alpha}, \rho v y^{\alpha}, \rho e y^{\alpha}, \rho c_1 y^{\alpha}, \ldots, \rho c_N y^{\alpha}\right\}$$

The F and G arrays contain flux terms (convective and diffusive), heat-transfer terms, and stress terms (normal and shear).[7,8] The H array contains source terms such as normal stresses σ_+ and the chemical production terms w_i for each specie:

$$H = \{0, 0, \alpha\sigma_+, 0, -w_1, \ldots, -w_N\}$$

The chemical production terms are computed using a chemical kinetics mechanism developed specifically for plasma/air chemistry.[5] The mechanism consists of 57 reactions and 39 species: electrons, C, C^+, C^{++}, C^-, CH, CH^+, CN, CN^+, CO, CO^+, C_2, C_2^+, H, H^+, H^-, H_2, H_2^+, N, N^+, NH, NH^+, NO, NO^+, N_2, N_2^+, O, O^+, OH, OH^+, O_2, O_2^+, H_2O, HO_2, H_2O_2, HNO_2, NO_2, CO_2, and O_3. An important simplifying assumption was made in constructing this mechanism, namely, only mixtures that had a concentration of O_2 greater than that of the plasma constituents were considered. As a result, the mixtures were assumed to be fuel lean in the combustion sense, the C and H containing species just mentioned being fuels. For a detailed discussion the reader is directed to Ref. 5.

Because no provisions have been made in the conservation equations [Eq. (1)] for flows with electric currents, the flowfield outside the capillary was rendered electrically neutral by setting the diffusion velocity of the electrons equal to the average diffusion velocity of the ions; the diffusion coefficient for the electrons is then computed from that of the ions. We realize that the plasma gas does not necessarily behave as a perfect fluid. Indeed the ionized gas is usually characterized as one in which Coulomb interactions between charged particles create significant departures from the perfect gas behavior. However, for weakly imperfect gases one can prescribe terms that account for Coulomb interactions as corrections to the classic pressure-density-temperature relations. Such corrections are described in Ref. 6. Alternately, it has been shown[9] that the property determinations obtained from the NASA-Lewis database[10] without modification, such as enthalpy and specific heats, are reasonably accurate and that the correction terms need not be employed. For a detailed discussion of the plasma properties, the reader is directed to Ref. 9.

The Navier–Stokes equations [Eq. (1)] are written in integral form and then reexpressed in a semidiscrete fashion using a finite volume discretization technique. The numerical computations proceed by solving the semidiscrete equation on each computational cell using central and upwind numerical differences along with flux limiting. Once properly discretized, the resulting set of algebraic equations are solved in a coupled manner in time using an explicit time-accurate method. The numerical time step is computed using the Courant–Friedrichs–Lewy condition. A separate chemical time step is computed as well. The final time step is based on the smallest of these. For a more complete description of the numerical scheme, the reader is referred to papers by Nusca[7] and Nusca et al.[8]

Experimental Effort

Litzinger et al.[11] at the Pennsylvania State University (PSU) have designed and operated the open-air experiment shown schematically in Fig. 1. The polyethylene capillary is typically 26 mm in length and 3 mm in diameter. An extension tube 26 mm in length is placed at the capillary exit, which serves as the cathode and guides the plasma efflux into the open air. The capillary and the extension tube are mounted within a solid housing (not shown in Fig. 1). An instrumented plate is placed at some distance L from the plasma device, typically 19 mm. Pressure probes are mounted on the plate with a spacing of 9.53 mm ($\frac{3}{8}$ in.).

Results and Discussion

The computational domain chosen to simulate the PSU experiment is shown in Fig. 2. This domain extends from the capillary/extender tube on the left to the plate on the right (19 mm) and from the centerline of the capillary (and plate) to a fixed radial distance (40 mm), which is determined by the distance from the plate centerline to the pressure probe designated P1 and includes a small radial distance beyond. This region was discretized using 154 axial grid cells and 295 radial grid cells, distributed with essentially even spacing throughout. Some degree of radial grid clustering was

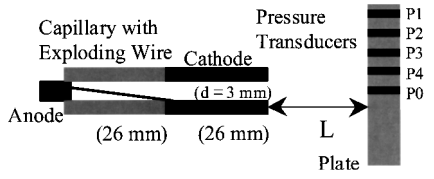

Fig. 1 Schematic of the Pennsylvania State University experimental setup (Ref. 11).

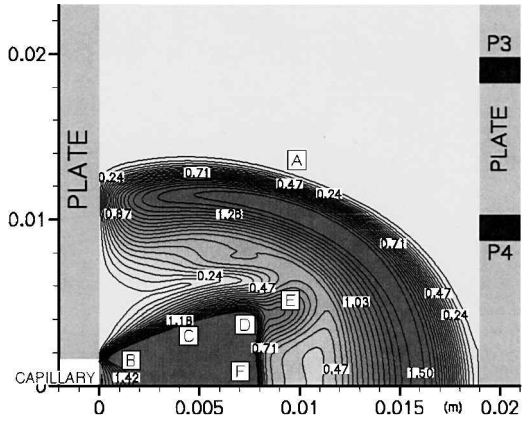

Fig. 2a Computed Mach-number contours (gray regions indicate Mach > 1), time = 0.03 ms.

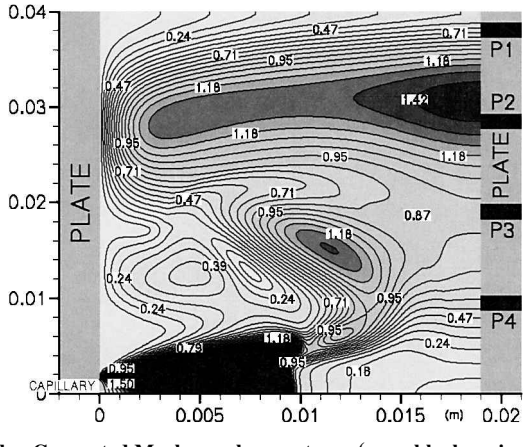

Fig. 2b Computed Mach-number contours (gray-black regions indicate Mach > 1), time = 0.07 ms.

used up to 0.015 m in order to resolve more accurately the formation of important gas dynamic phenomena (expansions, shocks, and turbulent mixing). Although the flowfield was modeled using viscous transport terms in the governing equations, no attempt was made to cluster grid points near the walls in order to resolve wall boundary layers. The simulation, run using a grid with twice the resolution, showed no significant effects on flow variables or shock resolution.

Initially, the entire flowfield is filled with air (0.8 mole fraction of N_2 and 0.2 mole fraction of O_2). The boundary conditions for the region are symmetry on the axis ($Y = 0$), outflow at $Y = 0.04$ m, and no penetration on both the capillary housing surface ($X = 0$, $0.0015 < Y < 0.04$ m) and on plate surface. Inflow conditions are specified at the capillary exit ($X = 0$, $0 < Y < 0.0015$ m). Given the current applied to the capillary (a "bell-shaped" time-dependent behavior over 0.25 ms with a peak of 9000 A) and the physical characteristics of the capillary (Fig. 1), the capillary model[6] generates the range of density (0.1–0.4 kg/m^3), velocity (6000–11,000 m/s), pressure (1–33 MPa), temperature (2000–30,000 K), and species distributions (see discussion of Fig. 3a). The inflow conditions for the computational domain follow from these values. Because the capillary is exhausting to ambient conditions, the rapid rise to peak efflux conditions (0.07 ms) causes the capillary exit to choke (Mach-number unity). The capillary and open-air domains are therefore isolated and can be modeled separately—the sonic capillary exit serving as the inflow boundary for the computational domain. Flow in the capillary is electrically charged, but the open-air efflux is modeled as electrically neutral.

The high pressure and temperature plasma efflux enters the open air as a highly underexpanded jet (see gray-scale contours in Fig. 2a with Mach numbers between 0, white, and 1.5+, black). The efflux of plasma from the inlet generates a weak precursor shock (A) that extends spherically. Behind this shock is air; the plasma is entirely contained by this shock and is separated from the air by an irregularly shaped contact surface across which pressure and velocity are preserved, but entropy changes discontinuously. Expansion waves, generated at the inlet (B), travel to the precursor shock (A), are reflected as weak compression waves, and coalesce into a strong oblique shock, or barrel shock (C). Because of the variable viscosity in the flowfield, the precursor shock is more diffuse than the Mach disk or the barrel shock. This barrel shock (C) terminates in an irregular reflection that forms a triple point (D) joining the barrel shock's (C) reflection (E), and a normal shock or Mach disk (F). Whereas the precursor shock (A) is relatively weak, producing a mildly supersonic flow, the barrel shock (C) and Mach disk (F) are strong shocks that enclose a fully supersonic flow.

The precursor shock reaches the plate at about 0.05 ms. By about 0.07 ms (see gray-scale contours in Fig. 2b with Mach numbers between 0, white, and 1.5+, black) the precursor shock is traversing the plate vertically. Stagnation of supersonic flow on the plate causes a shock reflection that moves back toward the capillary as the precursor shock travels along the plate. This causes the Mach disk to recede, settling at 0.01 m from the capillary (Fig. 2b).

Figure 4 shows the typical comparison for the P4 and the P1 tap locations. Predicted results for the P4 tap location (Fig. 4a) have been shifted in time by 0.022 ms in order to line up the arrival time for the precursor shock; the computed shock velocity is too high because the effects of translation of capillary residue (i.e., solid particles from the vaporization of the polyethylene liner) are absent in the simulation. With this adjustment the timing of subsequent pressure peaks are well predicted by the code, but the pressure levels are too low. The results for the P1 tap location (Fig. 4b) are also encouraging (no adjustments have been made) because the pressure peaks occur at regular time intervals for both predicted and measured data; however, the predicted pressures are too high. Figure 3 displays some of the chemical aspects of the flowfield. Figure 3b shows the time histories of the major species at the plate centerline (i.e., P0 tap location). Comparison of this figure with Fig. 3a

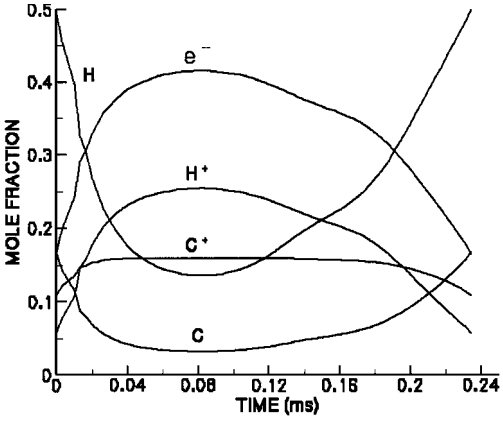

Fig. 3a Computed mole fraction histories at the capillary exit.

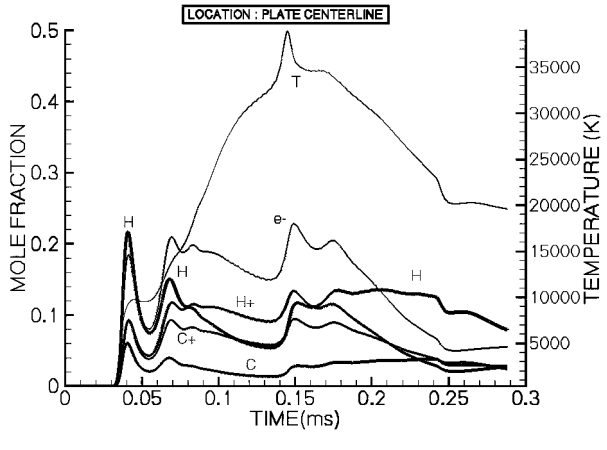

Fig. 3b Computed mole fraction histories at the plate centerline.

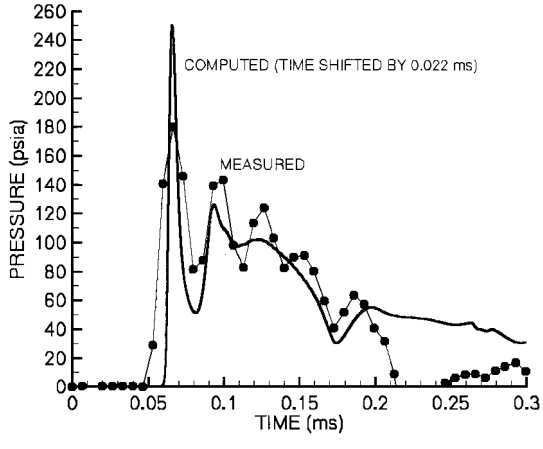

Fig. 4a Computed and measured pressure histories at tap location P4.

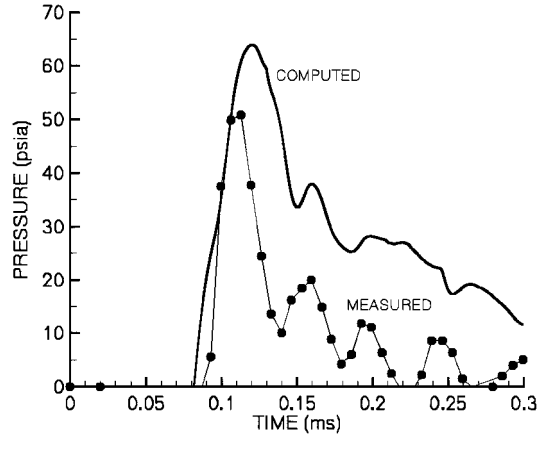

Fig. 4b Computed and measured pressure histories at tap location P1.

(distributions at the capillary exit) indicates that a large proportion of the ion species are actually deposited onto the plate, which are expected to ultimately affect the ignition and combustion characteristics of a propellant sample placed on the plate (future simulation). Of course, these results are dependent on the plasma/air chemical mechanism[5] employed in this study and therefore warrant further study. See Ref. 8 for a presentation and discussion of the complete set of computational results.

Conclusions

A time-accurate computational-fluid-dynamics code has been applied to the modeling of the high-temperature, chemically reactive plasma efflux from an ETC igniter fired into open air and impinging on an instrumented plate. The major features of this efflux have been resolved by numerical simulation, revealing a highly underexpanded jet with a strong precursor shock, a barrel shock that reflects at a triple point, and a Mach disk. Impact of the jet upon a plate generates a stagnation region, a reflected shock that travels back toward the capillary, and a normal shock that traverses the plate. Evidence of these phenomena is seen in both the experimental data and the predictions. Although the computed and measured pressures on the plate are quite similar in trend and magnitude, several observed discrepancies may be attributable to the thermochemical representation of the plasma in the governing equations, equation of state, and chemical kinetics mechanism.

References

[1]Del Guercio, M., "Propellant Burn Rate Modification by Plasma Injection," *Proceedings of the 34th JANNAF Combustion Subcommittee Meeting*, Vol. 1, edited by R. S. Fry and M. T. Gannaway, Johns Hopkins Univ., Columbia, MD, 1997, pp. 35–42.

[2]Dyvik, J. A., and Katulka, G., "ETC Temperature Compensation; Experimental Results of 120-mm Test Firings," *Proceedings of the 33rd JANNAF Combustion Subcommittee Meeting*, Vol. 3, edited by R. S. Fry and M. T. Gannaway, Johns Hopkins Univ., Columbia, MD, 1996, pp. 111–119.

[3]Katulka, G. L., and Dyvik, J., "Experimental Results of Electrical Plasma Ignition in 120-mm Solid Propellant Tank Gun Firings," *Proceedings of the 33rd JANNAF Combustion Subcommittee Meeting*, Vol. 3, edited by R. S. Fry and M. T. Gannaway, Johns Hopkins Univ., Columbia, MD, 1996, pp. 10–34.

[4]Nusca, M. J., and White, K. J., "Plasma Radiative and Convective Interactions with Propellant Beds," *Proceedings of the 34th JANNAF Combustion Subcommittee Meeting*, Vol. 1, edited by R. S. Fry and M. T. Gannaway, Johns Hopkins Univ., Columbia, MD, 1997, pp. 21–42.

[5]Anderson, W. R., and Schroeder, M. A., "Chemical Mechanism for ETC Plasma Interaction with Air," *Proceedings of the 36th JANNAF Combustion Subcommittee Meeting*, Vol. 2, edited by R. S. Fry and M. T. Gannaway, Johns Hopkins Univ., Columbia, MD, 1999, pp. 43–54.

[6]McQuaid, M. J., and Nusca, M. J., "Calculating the Chemical Compositions of Plasmas Generated by an Ablating-Capillary Arc Ignition System," *Proceedings of the 36th JANNAF Combustion Subcommittee Meeting*, Vol. 2, edited by R. S. Fry and M. T. Gannaway, Johns Hopkins Univ., Columbia, MD, 1999, pp. 143–158.

[7]Nusca, M. J., "Numerical Simulation of Electromagnetic Wave Attenuation in Nonequilibrium Chemically Reacting Flows," *Computers and Fluids*, Vol. 27, No. 2, 1998, pp. 217–238.

[8]Nusca, M. J., McQuaid, M. J., and Anderson, W. A., "Development and Validation of a Multi-Species Reacting Flow Model for the Plasma Jet Generated by an ETC Igniter," *Proceedings of the 37th JANNAF Combustion Subcommittee Meeting*, Vol. 1, edited by R. S. Fry and M. T. Gannaway, Johns Hopkins Univ., Columbia, MD, 2000, pp. 55–62.

[9]McQuaid, M. J., and Nusca, M. J., "Thermodynamic Property Characterization of Plasmas Generated by an Ablating-Capillary Arc," *Proceedings of the 37th JANNAF Combustion Subcommittee Meeting*, Vol. 1, edited by R. S. Fry and M. T. Gannaway, Johns Hopkins Univ., Columbia, MD, 2000, pp. 63–71.

[10]McBride, B. J., and Gordon, S., "Computer Program for Calculation of Complex Chemical Equilibrium Compositions and Applications, II. Users Manual and Program Description," NASA RP 1311, June 1996.

[11]Litzinger, T. A., Li, J-Q., Zhou, H., Kudva, G., and Thynell, S., "Plasma Propellant Interactions: Experiments and Modeling," *Proceedings of the 37th JANNAF Combustion Subcommittee Meeting*, Vol. 1, edited by R. S. Fry and M. T. Gannaway, Johns Hopkins Univ., Columbia, MD, 2000, pp. 36–45.